

Low-field magnetic anomalies in single crystals of the A-type square-lattice antiferromagnet EuGa_4

Santanu Pakhira ¹ and D. C. Johnston ^{1,2}¹*Ames National Laboratory, Iowa State University, Ames, Iowa 50011, USA*²*Department of Physics and Astronomy, Iowa State University, Ames, Iowa 50011, USA*

(Received 29 September 2022; accepted 9 January 2023; published 25 January 2023)

The body-centered-tetragonal antiferromagnet EuGa_4 was recently identified as a Weyl nodal-line semimetal that exhibits the topological Hall effect below its reported antiferromagnetic (AFM) ordering temperature $T_N = 15\text{--}16.5$ K which we find to be $T_N = 16.4(2)$ K. The Eu^{+2} ions are located at the corners and body centers of the unit cells. EuGa_4 exhibits A-type antiferromagnetic order below T_N , where the Eu^{2+} spin-7/2 moments are ferromagnetically aligned in the ab plane with the Eu moments in adjacent Eu planes along the c axis aligned antiferromagnetically. Low-field magnetization versus field $M(H_{ab})$ data at $T = 2$ K with the field aligned in the ab plane are reported that exhibit anomalous positive curvature up to a critical field H_{c1} at which a second-order transition occurs with $H_{c1} \approx 0.85$ kOe for $\mathbf{H} \parallel [1, 1, 0]$ and ≈ 4.8 kOe for $\mathbf{H} \parallel [1, 0, 0]$. For larger fields, the linear behavior $M_{ab} = \chi(T_N)H_{ab}$ is followed until the critical field H_c is reached at which all moments become aligned with the applied field. A theory is formulated for $T = 0$ K that fits the observed $M(H_{ab})$ behavior at $T = 2$ K well, where domains of A-type AFM order with fourfold rotational symmetry occur in the AFM state in zero field. The moments in the four domains reorient to become almost perpendicular to \mathbf{H}_{ab} at H_{c1} , followed by increasing canting of all moments toward the field with increasing field up to H_c which is reported to be 71 kOe. A first-order transition in $M(H_{ab})$ at $H_{ab} = H_{c1}$ is predicted by the theory for $T = 0$ K when \mathbf{H}_{ab} is at a small angle from the $[1, 0, 0]$ direction.

DOI: [10.1103/PhysRevB.107.024421](https://doi.org/10.1103/PhysRevB.107.024421)

I. INTRODUCTION

Antiferromagnets are fundamentally interesting owing to their various spin arrangements as well as their technological applications in spintronics, spin valves, magnetological devices, and spin-wave-based information technologies [1–4]. Recently, many antiferromagnetic (AFM) compounds have also been discovered to host nontrivial topological electronic and spin states [5–8]. Understanding the magnetic interactions in these materials is important for their further development and discovery of new materials. The magnetic ordering in those materials is primarily determined by the interplay of exchange interactions, magnetic anisotropy energy, and any kind of disorder present in the system. In particular, magnetocrystalline and magnetic-dipole anisotropies play a crucial role in tuning the spin arrangements in different AFM materials.

Among these materials, Eu-based antiferromagnets have been of significant interest recently due to the complex interplay of magnetism and topological states [6, 9–11]. EuX_4 -type of materials ($X = \text{Al}, \text{Ga}$) constitute one such family which is generating significant interest due to the recent observation of the topological Hall effect (THE) and related phenomena in these materials [12–14]. They crystallize in the body-centered-tetragonal (bct) BaAl_4 -type crystal structure (Fig. 1) with space group $I4/mmm$ [15], where the Eu atoms in each ab -plane layer form a square lattice and are known to exhibit a rich variety of magnetic and electronic properties. For

example, EuAl_4 orders antiferromagnetically below $T_N = 15$ K along with a charge density-wave (CDW) transition at $T_{\text{CDW}} = 140$ K [16–20]. The CDW transition is suppressed to $T = 0$ K by the application of a pressure of 2.5 GPa [18]. The isoivalent analog EuGa_4 also orders antiferromagnetically below $T_N \approx 16$ K and a CDW is only observed at $T_{\text{CDW}} = 105$ K under the application of a pressure $p = 0.75$ GPa [18, 21]. A THE is also evidenced in EuAl_4 coexisting with CDW order [12].

Although magnetic spin reorientation and multiple metamagnetic transitions were observed earlier in EuGa_2Al_2 [19], a recent observation of the THE and incommensurate magnetic order suggest the presence of a field-induced skyrmion-like topological spin texture in this compound [14]. A lack of inversion symmetry in noncentrosymmetric materials with Dzyaloshinskii-Moriya (DM) interactions was initially thought to be the key ingredient for stabilizing this spin texture. However, observations of a skyrmionic phase in centrosymmetric materials [8, 22, 23] have challenged the understanding and mechanism of this spin-texture formation. Contemporary theoretical modeling suggests that the interplay of different spin interactions and anisotropy may play a crucial role in the formation of a topological spin texture in centrosymmetric materials [24]. Thus, to understand the mechanism of complex spin texture and its field-induced evolution, it is necessary to study the magnetic properties and anomalous behavior in antiferromagnets with small anisotropy.

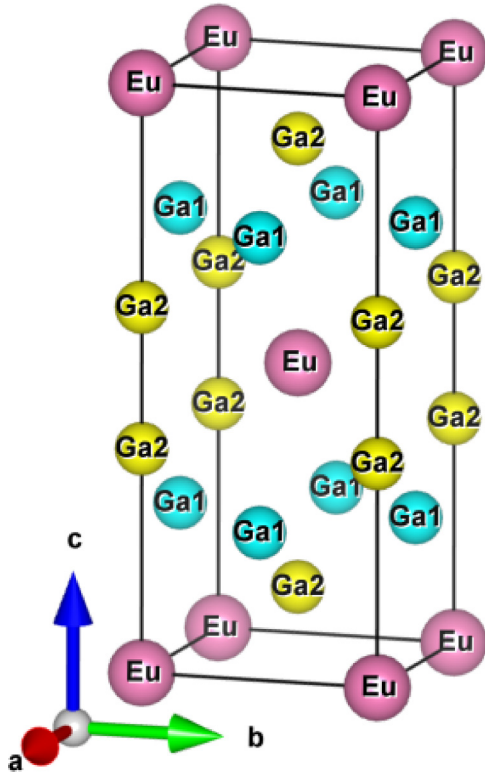


FIG. 1. Body-centered-tetragonal crystal structure of EuGa_4 . The Eu atoms form square lattices in the ab plane.

EuGa_4 exhibits giant magnetoresistance (MR) and THE with a possibility of magnetic skyrmions [13,25]. Recently, the observation of large transverse MR in this semimetal is explained due to the presence of Weyl nodal-line states and magnetic-field-induced Landau quantization [26]. As reported earlier, EuGa_4 exhibits collinear A-type AFM order below $T_N \approx 16$ K, where the Eu atoms are ferromagnetically aligned along the ab planes and adjacent FM planes along the c axis are aligned antiferromagnetically [17,18,21,25,27,28]. Although a noncollinear magnetic structure is favorable for skyrmion-like texture formation, the possibility of this texture in collinear EuGa_4 is quite intriguing where anisotropy can play an important role.

Previous magnetic studies on EuGa_4 mostly focused on the magnetic ground state and the high-magnetic-field behavior, while the low-field behavior and the effect of anisotropy was hardly explored. However, magnetization M versus applied magnetic field H isotherm measurements of a crystal with the field along the $[1,0,0]$ direction at $T = 2$ K revealed positive curvature up to a field $H_d = 5$ kOe, above which $M(H)$ was linear up to the critical field $H_{[1,0,0]}^c = 71$ kOe at which all moments become parallel to the field, whereas for the c -axis field, $M(H)$ was linear over the whole field range where $H_{[0,0,1]}^c = 72$ kOe (nearly isotropic) [21]. The authors suggested that this behavior was somehow associated with AFM domains that evolved into a single domain at H_d , and found that H_d decreased smoothly to zero on heating to T_N .

Here, we report studies of the magnetic-field evolution of the AFM ground-state spin texture at $T = 2$ K in detail emphasizing the low-field region. We found that

although the c -axis magnetization increases linearly with the applied field H , as expected and found for an A-type antiferromagnet, a nonlinear $M(H)$ response at low fields was observed for the $[1,0,0]$ field direction as previously found in Ref. [21]. Interestingly, we found that the low-field (ab)-plane nonlinearity differs significantly for fields in the $[1,0,0]$ and $[1,1,0]$ directions. On the basis of our temperature- and magnetic-field-dependent magnetic measurements complemented with theoretical analyses, we conclude that the ground-state A-type AFM structure consists of four equally-populated AFM domains having fourfold rotational symmetry associated with the fourfold ab -plane magnetic anisotropy of the ferromagnetic ab -plane layers. We propose a theory in which, with increasing field in the ab plane, the moments in each domain initially cant to become nearly perpendicular to the field at a critical field H_{c1} (H_d above) with no change in the physical domain boundaries. Then with a further increase of the magnitude of the field all moments progressively cant towards the field giving rise to the observed linear $M(H)$ behavior up to the critical field H_c noted above. Our fits describe the experimental $M(H)$ isotherms at $T = 2$ K for $H \parallel [1, 0, 0]$ and $H \parallel [1, 1, 0]$ with $H \leq H_{c1}$ rather well, but where the H_{c1} values for the two field directions are quite different.

The experimental details are given in Sec. II. The experimental results are presented in Sec. III, including magnetic susceptibility $\chi(T)$ data in Sec. III A and magnetization versus field $M(H)$ isotherms in Sec. III B. Theoretical fits to the experimental $M(H)$ data at $T = 2$ K are presented in Sec. IV and concluding remarks are given in Sec. V.

II. EXPERIMENTAL DETAILS

EuGa_4 single crystals were grown using EuGa_9 self-flux. The high-purity elements (Eu metal from Ames Laboratory and 99.99999%-pure Ga from Alfa Aesar) were loaded in an alumina crucible and sealed in a silica tube. The ampule was then heated to 750 °C at a rate of 100 °C/h and held for 12 h. Then it was slowly cooled to 400 °C at a rate of 2 °C/h. The crystals were obtained after removing the flux using a centrifuge. The sample homogeneity and chemical composition were confirmed using a JEOL scanning electron microscope (SEM) equipped with an EDS (energy-dispersive x-ray spectroscopy) analyzer. The EDS measurements yielded a composition $\text{EuGa}_{4.04(2)}$, close to the stoichiometric composition. Magnetic measurements were carried out using a Magnetic Properties Measurement System (MPMS) from Quantum Design, Inc. We use cgs magnetic units throughout.

III. EXPERIMENTAL RESULTS

A. Magnetic susceptibility

The $\chi(T)$ data for EuGa_4 obtained with in-plane (χ_{ab} , $H \parallel ab$) and out-of-plane (χ_c , $H \parallel c$) magnetic fields $H = 0.1$ kOe are shown in Fig. 2, where χ_{ab} is measured for the two symmetry directions $H \parallel [1, 0, 0]$ and $H \parallel [1, 1, 0]$. The data in the figure indicate that χ is nearly isotropic in the ab plane. As seen from the figure, EuGa_4 undergoes an AFM transition at $T_N = 16.4(2)$ K, similar to values reported earlier [17,18,21,25,27,28]. The χ_c is found to be independent

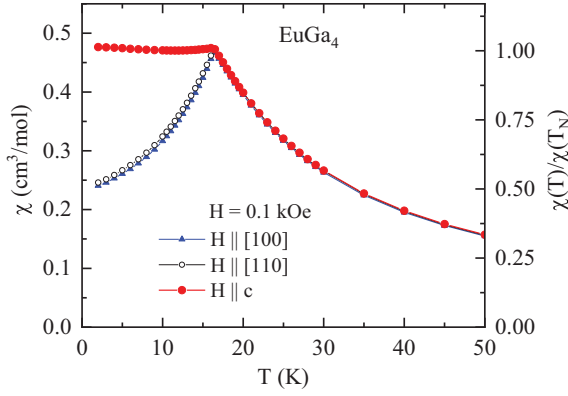


FIG. 2. Left ordinate: Temperature dependence of the magnetic susceptibility $\chi(T)$ of EuGa_4 for $H = 0.1$ kOe with $H \parallel ab \parallel [1, 0, 0]$ (filled blue triangles), $H \parallel ab \parallel [1, 1, 0]$ (open black circles), and $H \parallel c$ (filled red circles). The corresponding susceptibility ratio $\chi(T)/\chi(T_N)$ is shown on the right ordinate.

of T for $T \leq T_N$, indicating that the moments are aligned perpendicular to the c axis. This is consistent with the χ_{ab} data that decrease with decreasing T with $\chi_{ab}(2 \text{ K})/\chi(T_N) \approx 0.5$. According to molecular-field-theory (MFT) [29,30] for a c -axis helix of identical crystallographically-equivalent Heisenberg spins, one has

$$\frac{\chi_{ab}(T=0)}{\chi_{ab}(T_N)} = \frac{1}{2[1 + 2 \cos(kd) + 2 \cos^2(kd)]}, \quad (1)$$

where k is the magnitude of the c -axis AFM propagation vector, d is the distance along the c axis between the FM layers of spins, and hence kd is the turn angle between adjacent layers of spins.

The ratio on the left side of Eq. (1) for $\mathbf{H} \parallel [1, 0, 0]$ at $T = 2 \text{ K}$ was previously found to be $\approx 0.26/0.51 \approx 0.51$ [21]. According to Fig. 2, as noted above we find the similar value

$$\frac{\chi_{[1,0,0]}(T=2 \text{ K})}{\chi(T_N)} \approx \frac{0.24}{0.48} \approx \frac{1}{2}. \quad (2)$$

Using this value of $\chi_{ab}(2 \text{ K})/\chi_{ab}(T_N)$, Eq. (1) yields the turn angle between the moment directions in adjacent Eu layers to be $kd = \pi$ rad, indicating that the AFM structure is A-type, in agreement with the earlier neutron-diffraction solution of the magnetic structure of EuGa_4 [27].

The inverse molar magnetic susceptibility $1/\chi$ for $H = 0.1 \text{ T}$ is plotted versus T for $H \parallel [1, 0, 0]$ in Fig. 3(a) and $H \parallel [0, 0, 1]$ in Fig. 3(b). Both plots are linear above T_N and are described well by the inverse of the modified Curie-Weiss law

$$\chi(T) = \chi_0 + \frac{C}{T - \theta}, \quad (3)$$

where χ_0 is the T -independent contribution, C is the molar Curie constant and θ is the Weiss temperature. The fits yield the values of these variables in Table I. The magnitudes of the diamagnetic χ_0 values are of the order expected for the diamagnetic core contributions but are very small relative to the χ values of the Eu^{2+} moments. The listed effective moments μ_{eff} for the two field directions are close to the theoretical value of $7.94 \mu_B/\text{Eu}^{2+}$ for $g = 2$ and $S =$

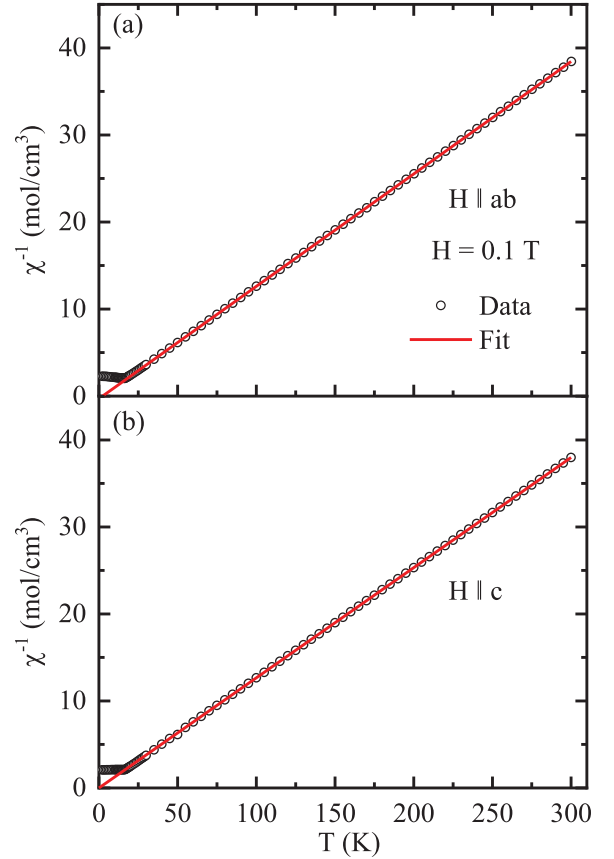


FIG. 3. Inverse magnetic susceptibility $\chi^{-1}(T)$ of EuGa_4 with $H = 0.1 \text{ T}$ for (a) $H \parallel ab$ and (b) $H \parallel c$.

$7/2$. The Weiss temperatures are positive, consistent with the A-type AFM structure in which FM planes of Eu spins are stacked antiferromagnetically along the c axis. However, they are not close to the value of T_N , indicating that the AFM interactions between the Eu spins in adjacent layers perpendicular to the c axis are also significant.

Indeed, using the above experimental data together with molecular-field theory (MFT) for a c -axis helix, the three Heisenberg exchange constants J_0 (the sum of the exchange constants between a spin and all other spins in the same FM-aligned layer in the ab plane), J_1 (the sum of all exchange constants between a spin and all spins in an adjacent FM-aligned layer along the c axis), and J_2 (the sum of all exchange constants between a spin and all spins in a next-nearest layer) can be obtained by solving the following three

TABLE I. The fitted parameters to the inverse susceptibility data in Fig. 3, including the T -independent contribution to the susceptibility χ_0 , molar Curie constant C_α for $\alpha = ab, c$ directions, effective moment per Eu spin $\mu_{\text{eff}} \approx \sqrt{8C_\alpha}$, and the Weiss temperature θ_α .

Field direction	χ_0 ($10^{-5} \frac{\text{cm}^3}{\text{mol}}$)	C_α ($\frac{\text{cm}^3 \text{K}}{\text{mol}}$)	$\mu_{\text{eff}\alpha}$ ($\frac{\mu_B}{\text{Eu}}$)	θ_α (K)
$H \parallel ab$	-1.7(5)	7.76(1)	7.88(1)	2.27(6)
$H \parallel c$	-3.5(3)	7.86(1)	7.93(1)	0.5(1)

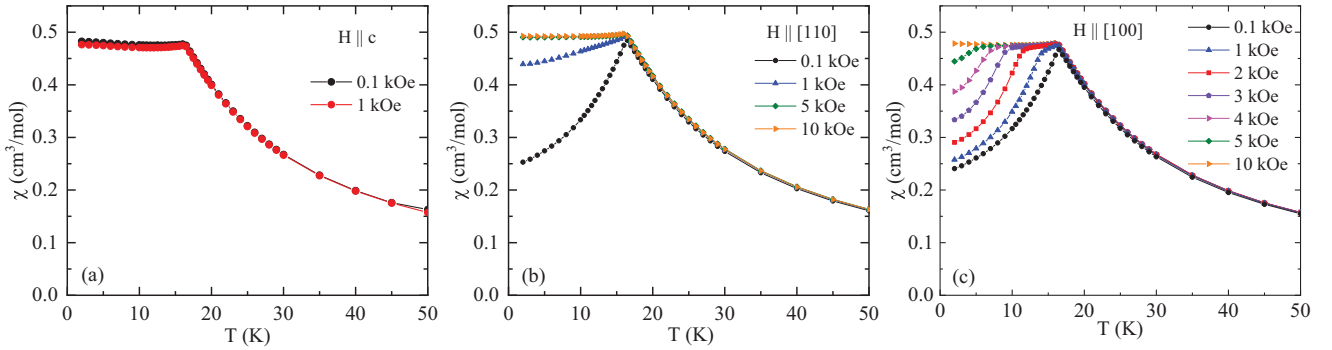


FIG. 4. (a) Out-of-plane magnetic susceptibility $\chi_c(T)$ ($H \parallel c$) of EuGa_4 for different applied magnetic fields. In-plane magnetic susceptibility for different magnetic fields for (b) $H \parallel ab \parallel [1, 1, 0]$ and (c) for $H \parallel ab \parallel [1, 0, 0]$. The field responses in these two ab -plane symmetry directions are seen to be significantly different.

simultaneous equations [30]:

$$\begin{aligned} \cos(kd) &= -\frac{J_1}{4J_2}, \\ T_N &= -\frac{S(S+1)}{3k_B} [J_0 + 2J_1 \cos(kd) + 2J_2 \cos(2kd)], \\ \theta &= -\frac{S(S+1)}{3k_B} (J_0 + 2J_1 + 2J_2). \end{aligned} \quad (4)$$

For EuGa_4 the required parameter values are $S = 7/2$, $kd = \pi$ rad for A-type antiferromagnetism with the moments aligned in the ab plane, $T_N = 16.4$ K, and the average Weiss temperature $\theta_{\text{ave}} = 1.6$ K from Table I. Neglecting the weak ab -plane anisotropy discussed above and solving Eq. (4) yield the Heisenberg exchange constants in temperature units as $J_0 = -2.1$ K (FM), $J_1 = 0.71$ K (AFM), and $J_2 = 0.18$ K (AFM). This confirms that significant AFM exchange interactions are present in EuGa_4 , in addition to the FM ab -plane exchange interactions necessary for the Eu moments to align ferromagnetically in the ab plane.

The magnetic-field dependences of $\chi(T)$ are shown in Fig. 4 for (a) $H \parallel c$, (b) $H \parallel [1, 1, 0]$ and (c) $H \parallel [1, 0, 0]$. No change in $\chi_c(T)$ is observed between $H = 0.1$ and 1 kOe. However, a significant variation of $\chi_{ab}(T)$ is observed in this field region. Interestingly, the field evolution of $\chi_{ab}(T)$ at low fields is quite different when the magnetic field is applied along the ab plane $[1, 0, 0]$ and $[1, 1, 0]$ directions. The critical fields at which the moments become aligned with the applied field are at much higher fields $H_{ab}^c = 71$ kOe and $H_c^c = 72$ kOe for $H \parallel ab$ and $H \parallel c$, respectively [21], indicating a very small magnetic anisotropy between these two field directions as expected for Eu^{2+} moments with spin $S = 7/2$ and angular-momentum quantum number $L = 0$.

The $\chi_{ab}(T)$ in Fig. 4(b) for $T \leq T_N$ strongly increases between applied fields $H = 0.1$ and 1 kOe applied along the $[1, 1, 0]$ direction and at higher fields it becomes independent of T . On the other hand, only a gradual increase in $\chi_{ab}(T)$ with increasing H is observed for $H \parallel [1, 0, 0]$ in Fig. 4(c) in the field range $0.1 \text{ kOe} \leq H \lesssim 5 \text{ kOe}$. Moreover, a T -independent region of $M(H)$ is observed for $H = 1$ kOe for $H \parallel [1, 0, 0]$ and the temperature range of that plateau increases with increasing H . Finally, $\chi(T)$ for both $H \parallel [1, 0, 0]$ and $H \parallel [1, 1, 0]$ in the AFM state below T_N

becomes independent of T for $H = 10$ kOe. We show in Sec. IV below that the different low-field $M(H)$ behavior of $\chi_{ab}(H)$ for $H \parallel [1, 0, 0]$ and $H \parallel [1, 1, 0]$ in EuGa_4 is due to AFM domain formation arising from the fourfold tetragonal c -axis rotational symmetry. Similar effects were found previously in trigonal Eu-based compounds with threefold rotational symmetry about the c axis [31–35].

B. Magnetization versus Field Isotherms

In order to provide further insight into the field-dependent evolution of the magnetic behavior at $T < T_N$, $M(H)$ isotherm data were obtained that emphasize the low-field region of interest. As can be seen in Fig. 5, the $M(H)$ behavior measured at $T = 2$ K for $H \parallel c$ is linear. In accordance with the magnetic susceptibility measurements, a clear nonlinear response in $M(H)$ is observed for both $H \parallel [1, 0, 0]$ and $H \parallel [1, 1, 0]$. This is clearly reflected in the dM/dH data, where dM/dH initially increases rapidly with increasing H and exhibits peaks at the critical fields $H_{c1,[1,0,0]} \approx 4.8$ kOe and $H_{c1,[1,1,0]} \approx 0.85$ kOe, followed eventually by an H -

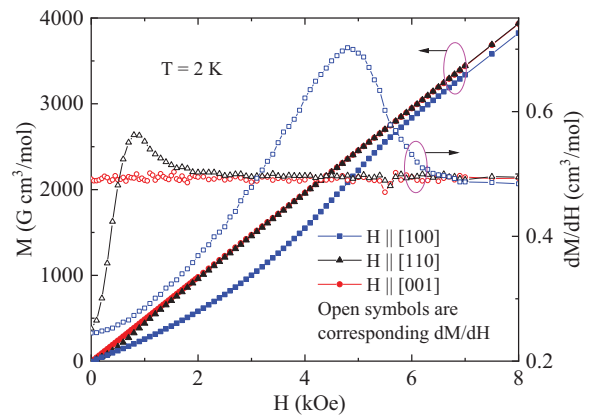


FIG. 5. Low-field $M(H)$ data measured at $T = 2$ K for $H \parallel [1, 0, 0]$, $H \parallel [1, 1, 0]$, and $H \parallel [0, 0, 1]$ (left ordinate). The corresponding field derivatives are also plotted (open symbols, right ordinate). Although $M_c(H)$ for $H \parallel [0, 0, 1]$ is linear, distinct nonlinearities in $M_{ab}(H)$ for $H \parallel [1, 0, 0]$ and $[1, 1, 0]$ are observed in this low-field region.

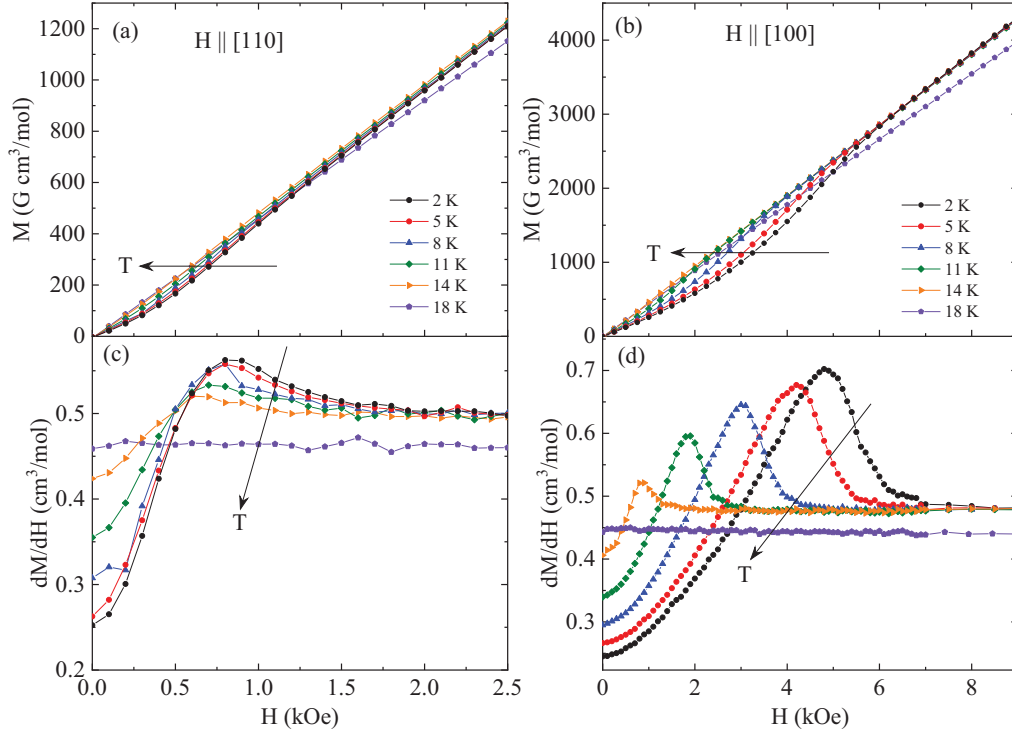


FIG. 6. In-plane $M(H)$ data measured at different temperatures for (a) $H \parallel [1, 1, 0]$ and (b) $H \parallel [1, 0, 0]$. The respective $dM(H)/dH$ vs H data are shown in (c) and (d). The data for $T = 18$ K are about 2 K above T_N .

independent behavior for $H > H_{c1}$. The difference in the low-field $M(H)$ behavior for different in-plane symmetry directions can be explained by the rotation of the moments in ab -plane AFM domains as discussed in detail in Sec. IV below.

The $M(H)$ data measured at different temperatures for $H \parallel [1, 1, 0]$ are shown in Fig. 6(a) and the corresponding dM/dH versus H data are plotted in Fig. 6(c). As seen in the latter figure, H_{c1} slightly shifts to lower fields with increasing temperature below T_N , with $H_{c1,[1,1,0]} = 0.85$ kOe at $T = 2$ K decreasing to 0.6 kOe at $T = 14$ K. The $M(H)$ behavior is linear for $T > T_N$. The T dependences of $M(H)$ and $dM/dH(H)$ for $H \parallel [1, 0, 0]$ are shown in Figs. 6(b) and 6(d), respectively. Here, the nonlinearity in $M(H)$ at $T = 2$ K persists up to $H \approx 8$ kOe, which is much larger than that observed for $H \parallel [1, 1, 0]$. The dM/dH for this field direction shows a maximum at $H_{c1,[1,0,0]} = 4.8$ kOe at $T = 2$ K. This critical field is significantly reduced to $H_{c1,[1,0,0]} = 0.85(5)$ kOe at $T = 14$ K. The striking difference observed in the $M(H)$ and corresponding dM/dH behavior between the $H \parallel [1, 1, 0]$ and $H \parallel [1, 0, 0]$ directions indicates the presence of significant in-plane magnetic anisotropy. This anisotropy is associated with the magnetic-field-induced moment reorientation in the AFM domains discussed below in Sec. IV.

We tested the reversibility of the nonlinear $M(H)$ and dM/dH at low fields upon heating and cooling for $H \parallel [1, 0, 0]$. The crystal was initially cooled to $T = 2$ K under a magnetic field $H = 50$ kOe. After T stabilization, $M(H)$ was measured in the hysteresis H cycle 10 kOe \rightarrow 0 kOe \rightarrow 10 kOe, as shown in Fig. 7. No magnetic hysteresis was observed, indicating that the low-field-induced $M(H)$ nonlinearity is reversible.

Similar $M_{ab}(H)$ behavior was observed for the Eu-based trigonal compounds EuMg_2Bi_2 and EuMg_2Sb_2 [31,32,34,35] and we successfully modeled those results [33] using an approach similar to that used below to model the low-field $M(H)$ data for EuGa_4 .

IV. FITS TO THE EXPERIMENTAL $M(H)$ DATA

A. Theory

The fourfold rotational magnetic-anisotropy free energy E_{anis} for the ferromagnetic ab -plane layers in tetragonal EuGa_4 versus the azimuthal angle ϕ of the ferromagnetic

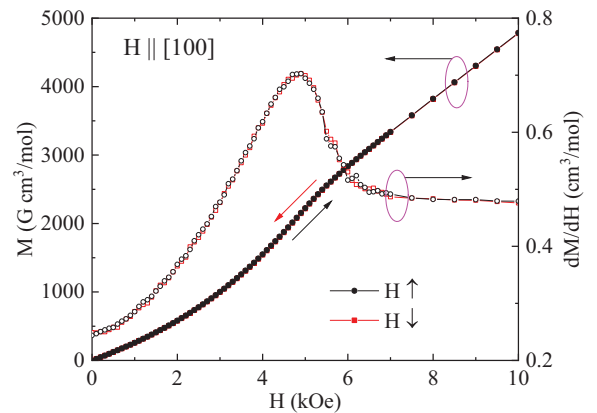


FIG. 7. In-plane field-cooled $M(H)$ behavior at $T = 2$ K for $H \parallel [1, 0, 0]$ in the hysteresis H cycle 10 kOe \rightarrow 0 \rightarrow 10 kOe. No hysteretic behavior is observed. The corresponding $dM(H)/dH$ behavior is also shown in the right ordinate.

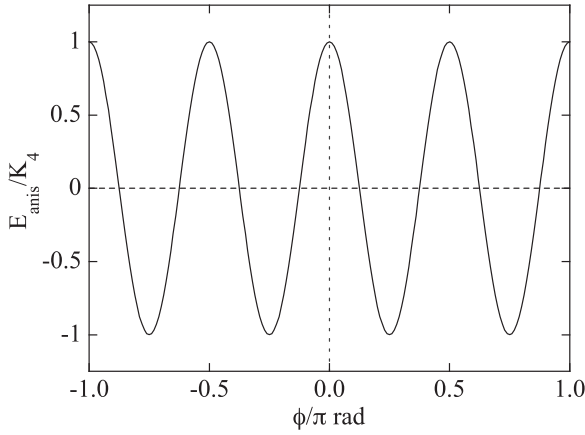


FIG. 8. Fourfold ab -plane rotational anisotropy energy normalized by the anisotropy constant K_4 , E_{anis}/K_4 , vs the ab -plane angle ϕ/π rad of a moment in tetragonal EuGa_4 .

moments in that layer is given by [36]

$$E_{\text{anis}} = K_4 \cos(4\phi), \quad (5)$$

where $K_4 > 0$ is the fourfold ab -plane anisotropy constant and ϕ is the angle of the moments with respect to the x axis defined in Fig. 9 below. A plot of E_{anis}/K_4 versus ϕ is shown in Fig. 8. The anisotropy-energy minima occur at $\phi = \pm\pi/4$ and $\pm 3\pi/4$ rad.

In order to model the anomalous low-field $M_{ab}(H)$ behavior for EuGa_4 in Figs. 5–7, we propose that the magnetic structure in $H = 0$ contains four equally-populated domains A, B, C, D of ferromagnetically-aligned moments in the A-type AFM structure illustrated in Fig. 9(a) as required by the tetragonal lattice symmetry. As shown in Fig. 9(a), each of the four domains contains moments that are ferromagnetically aligned in every-other ab plane and the moments in adjacent layers along the c axis are aligned at 180° with respect to the former moments, as required for an A-type AFM structure. We assume that within each physical AFM domain, the applied field H_x rotates the moments only in the ab plane and does not cause domain-wall motion. The former assumption is justified because in a body-centered-tetragonal lattice, the magnetic-dipole interaction favors ferromagnetic moment alignment in the ab plane rather than along the c axis [37]. As noted at the bottom of Fig. 9(a), the x direction of the applied field can be aligned along either the crystallographic $[1,0,0]$ or $[1,1,0]$ directions which may have different anisotropy energies.

In $H_x = 0$, the angles of moments 1, 3, 5, and 7 with respect to the x axis in the respective ferromagnetically-aligned layer are in energy minima according to Fig. 8. Similarly, moments 2, 4, 6, and 8 in either of the two layers of the A-type AFM structure adjacent to the respective layers containing moments 1, 3, 5, and 7 are also in energy minima. On application of H_x , due to the relationship of the directions of the moments in the different domains in Fig. 9(a) to each other, the magnitude of the change of the moment angle $\Delta\phi$ is the same for the moments in each domain as shown in the figure. During this process, the moments in adjacent ferromagnetically-aligned layers retain their 180° alignment due to the AFM exchange

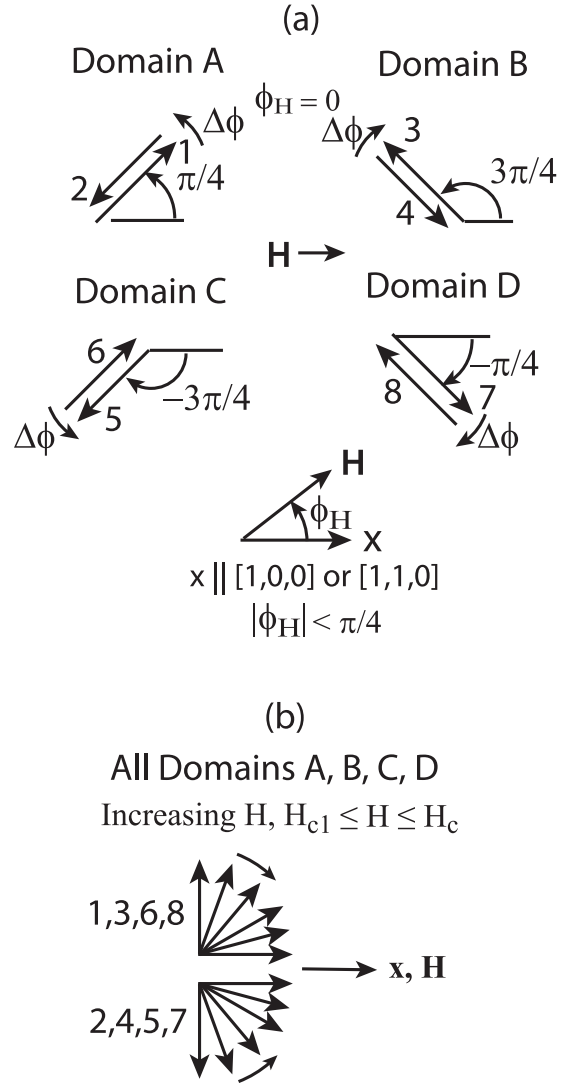


FIG. 9. (a) Schematic diagram of the nearly-locked moment orientations in the ab plane of adjacent antiparallel layers of moments along the c axis in the four collinear A-type AFM domains A, B, C, and D and their magnetic field evolution with increasing x -axis field H at low fields $H \leq H_{c1}$ shown by arrows. (b) For $H_x > H_{c1}$, each moment increasingly cant towards the increasing field as shown, until at the critical field H_c all moments are aligned with the field with $\mu_x = \mu_{\text{sat}} = gS\mu_B = 7\mu_B$.

interaction between moments in adjacent layers, apart from a very small canting towards the field which gives rise to the observed magnetization.

The moments in each domain eventually rotate to become perpendicular to H_x at a critical field H_{c1} at which a maximum is observed in dM_{ab}/dH in Figs. 5–7. For $H_x > H_{c1}$, the moments in each domain increasingly cant towards the applied field direction as shown in Fig. 9(b). The magnetization saturates when all the moments become parallel to the applied field H_x at a critical field H_c . As noted at the bottom of Fig. 9(a), it is possible to align \mathbf{H} at an angle $\phi_H \neq 0$ with respect to the positive x axis. As illustrated later, at $T = 0$ K this is predicted to result in a first-order transition at H_{c1} .

For $0 \leq H_x \leq H_{c1}$, from Fig. 9(a) the angles of the moments in each domain with respect to the positive x axis are respectively

$$\begin{aligned}\phi_A &= \frac{\pi}{4} + \Delta\phi, \\ \phi_B &= \frac{3\pi}{4} - \Delta\phi \\ \phi_C &= -\frac{3\pi}{4} + \Delta\phi, \\ \phi_D &= -\frac{\pi}{4} - \Delta\phi,\end{aligned}\quad (6)$$

where $0 \leq \Delta\phi \leq \pi/4$. The average anisotropy energy per domain for $0 \leq H_x \leq H_{c1}$ obtained using Eqs. (5) and (6) is

$$E_{\text{anis ave}} = -K_4 \cos(4\Delta\phi). \quad (7)$$

In a magnetic field H_x directed to the right as in Fig. 9(a), the magnetization component of a pair of collinear antiparallel moments along the axis of the moments at $T = 0$ K is zero according to molecular-field theory. On the other hand, the magnetization component perpendicular to either moment in H_x is $\mu_{\perp} = \chi_{\perp} H_{x\perp} = \chi_{\perp} H_x \sin(\phi_n)$, where $H_{x\perp} = H_x \sin(\phi_n)$, thus yielding

$$\begin{aligned}E_{\text{mag } n} &= -\mu_x H_x \\ &= -[\chi_{\perp} H_x \sin(\phi_n)][H_x \sin(\phi_n)] \\ &= -\chi_{\perp} H_x^2 \sin^2(\phi_n).\end{aligned}\quad (8a)$$

Summing $E_{\text{mag } n}$ over the angles of a moment in each of the four domains in Eq. (6) and dividing by four gives the average magnetic energy per moment for $0 \leq H_x \leq H_{c1}$ as

$$E_{\text{mag ave}} = -\frac{\chi_{\perp} H_x^2}{2} [1 + \sin(2\Delta\phi)]. \quad (8b)$$

Then using Eq. (7) and normalizing the total energy per moment by K_4 gives the total average energy per moment as

$$\begin{aligned}E_{\text{ave}}/K_4 &= (E_{\text{anis ave}} + E_{\text{mag ave}})/K_4 \\ &= -\cos(4\Delta\phi) - \frac{\chi_{\perp} H_x^2}{2K_4} [1 + \sin(2\Delta\phi)].\end{aligned}\quad (8c)$$

Now defining the dimensionless parameter h_x as

$$h_x = \frac{\chi_{\perp} H_x^2}{K_4}, \quad (9)$$

setting the derivative of E_{ave}/K_4 with respect to $\Delta\phi$ in Eq. (8c) equal to zero corresponding to the minimum energy E_{ave}/K_4 and solving the resultant equation for $\Delta\phi$ gives

$$\begin{aligned}\Delta\phi(\text{rad}) &= \frac{1}{2} \arctan\left(\frac{h_x}{\sqrt{64 - h_x^2}}\right) \quad (h_x \leq 8) \\ &= \frac{\pi}{4} \quad (h_x \geq 8),\end{aligned}\quad (10)$$

as plotted in Fig. 10 where the value 8 in Eq. (10) is exact. The maximum value $\Delta\phi = \pi/4$ rad is the value at which all moments become perpendicular to the applied field $H_x = H_{c1}$, apart from a small canting of the moments towards the field that gives rise to the measured magnetization along the x axis.

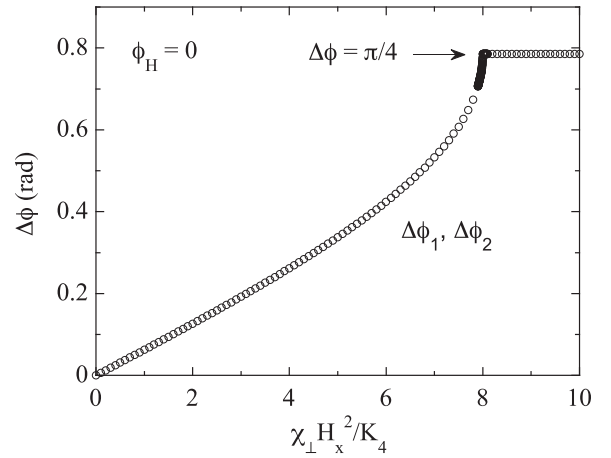


FIG. 10. The angle $\Delta\phi$ in Fig. 9(a) vs $h_x = \chi_{\perp} H_x^2 / K_4$ for $\phi_H = 0$ rad as defined at the bottom of Fig. 9(a).

At larger fields up to the critical field H_c , the individual moments increasingly cant towards the field and molecular-field theory predicts $M_{\perp} = \chi_{\perp} H_x = \chi(T_N) H_x$ until the critical field H_c is reached at which all the moments are aligned with the applied field \mathbf{H} as illustrated in Fig. 9(b).

Equation (10) and Fig. 10 show that the value of $\chi_{\perp} H_x^2 / K_4$ at the critical field H_{c1} for which $\Delta\phi = \pi/4$ rad is first reached is given by

$$\frac{\chi_{\perp} H_{c1}^2}{K_4} = 8. \quad (11a)$$

This equation gives the value of the anisotropy constant K_4 in terms of measurable quantities as

$$K_4 = \frac{\chi_{\perp} H_{c1}^2}{8}. \quad (11b)$$

Since K_4 is normalized to a single moment, whereas the measured χ_{\perp} is normalized to a mole of moments, this difference can be taken into account by writing Eq. (11b) as

$$K_4 = \frac{\chi_{\perp} H_{c1}^2}{8N_A}, \quad (11c)$$

where N_A is Avogadro's number. For EuGa_4 , the measured values are

$$\begin{aligned}\chi_{\perp}(T = 0 \text{ K}) &= \chi_c(T_N) = \chi_{ab}(T_N) \\ &= 0.48 \text{ cm}^3/\text{mol}\end{aligned}\quad (12)$$

according to molecular-field theory [30], and $H_{c1} \approx 4.8$ kOe for $H_x \parallel [1, 0, 0]$, yielding

$$K_4 = 1.4 \times 10^{-3} \frac{\text{meV}}{\text{Eu atom}}. \quad (13)$$

This value is of order 20–100 times larger than the values of the threefold anisotropy constants $K_3 = 6.5 \times 10^{-5}$ and $1.8 \times 10^{-5} \frac{\text{meV}}{\text{Eu atom}}$ obtained for trigonal EuMg_2Bi_2 and EuMg_2Sb_2 , respectively [33].

B. Fits of the M(H) data at T = 2 K by theory

The magnetization M_x per mole of Eu moments at $T = 0$ K versus magnetic field H_x averaged over a moment in each of

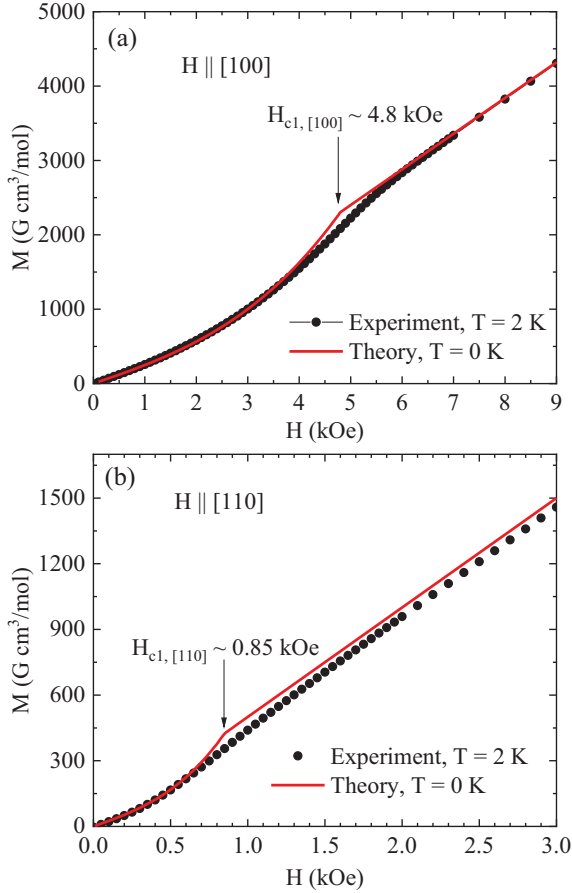


FIG. 11. The experimental ab -plane $M(H)$ behavior for two applied field directions (a) $H \parallel [1, 0, 0]$ and (b) $H \parallel [1, 1, 0]$ measured at $T = 2$ K along with theoretical predictions for $T = 0$ K with $H_{c1} \approx 4.8$ kOe and 0.85 kOe, respectively, as shown by the respective solid red curves. For $H > H_{c1}$, $M(H) = \chi(T_N)H$ is plotted according to molecular-field theory [30] which agrees very well with the slope of the data and is not a fit to the slope.

the two unique domains A and B in Fig. 9(a) is calculated from

$$M_{x\text{ave}} = \frac{\chi_{\perp} H_x}{2} [\sin^2(\phi_A) + \sin^2(\phi_B)] \quad (H_x \leq H_{c1})$$

$$= \frac{\chi_{\perp} H_x}{2} [1 + \sin(2\Delta\phi)], \quad (14a)$$

$$M_{x\text{ave}} = \chi_{\perp} H_x \quad (H_{c1} \leq H_x \leq H_c). \quad (14b)$$

Here ϕ_A and ϕ_B are given by the respective expressions in Eqs. (6), $\Delta\phi(h_x)$ is given by Eq. (10) with K_4 given in Eq. (13), and the value of χ_{\perp} is given in Eq. (12).

The experimental $M_{ab}(H)$ data for $H_x \parallel [1, 0, 0]$ and $H_x \parallel [1, 1, 0]$ at $T = 2$ K along with the calculated theoretical $M_x(H)$ behavior using Eqs. (10) and (14a) corresponding to $T = 0$ K are shown in Figs. 11(a) and 11(b), respectively. The value of H_{c1} is seen to be quite different for the two field directions. The theory reproduces the experimental data rather well at low fields $H \lesssim H_{c1}$, but deviates somewhat from the data for $H \gtrsim H_{c1}$. The reason for this discrepancy is not clear at present but may be associated with the fact that the theoretical calculations are done for $T = 0$ K, whereas the

observed $M_x(H)$ data were obtained at $T = 2$ K. A larger discrepancy between the theoretical and experimental data taken at $T = 1.8$ K was observed earlier for trigonal EuMg_2Bi_2 and EuMg_2Sb_2 , where the measurement temperatures were $T \approx 0.27 T_N$ and $\approx 0.23 T_N$, respectively. The discrepancy is smaller for EuGa_4 with measurement temperature $T \approx 0.13 T_N$. This occurs because the $T = 0$ K theoretical predictions are expected to agree best with experimental $M(H)$ data taken at temperature T when the ratio T/T_N is smallest.

We have also calculated the $M(H)$ behavior when H_x is not along the x axis parallel to the $[1,0,0]$ direction, but is in a direction in the ab plane where \mathbf{H} is at an arbitrary positive angle $\phi_H < \pi/4$ with respect to the $+x$ ($[1,0,0]$) axis as indicated at the bottom of Fig. 9(a). In this case, there are effectively two domains A and B, because $\phi_C = -\phi_B$ and $\phi_D = -\phi_A$ in Fig. 9(a). Setting $\phi_1 = \phi_A$ and $\phi_2 = \phi_B$, we therefore minimize the energy only with respect to ϕ_1 and ϕ_2 . The angles of the two domains for $0 \leq H_x \leq H_{c1}$ with respect to ϕ_H are

$$\phi_1 - \phi_H = \frac{\pi}{4} + \Delta\phi_1 \quad (0 \leq \Delta\phi_1 \leq \pi/4 + \phi_H),$$

$$\phi_2 - \phi_H = -\frac{\pi}{4} - \Delta\phi_2. \quad (0 \leq \Delta\phi_2 \leq \pi/4 - \phi_H). \quad (15)$$

The average anisotropy energy associated with the two domains is

$$E_{\text{anis ave}} = -\frac{K_4}{2} [\cos(4\phi_1) + \cos(4\phi_2)]. \quad (16)$$

The average magnetic energy in the regime $0 \leq H_x \leq H_{c1}$ is given by

$$E_{\text{mag ave}} = -\frac{\chi_{\perp} H_x^2}{2} [\sin^2(\phi_1 - \phi_H) + \sin^2(\phi_2 - \phi_H)]$$

$$= -\frac{\chi_{\perp} H_x^2}{4} [2 + \sin[2(\phi_1 - \phi_H)]$$

$$+ \sin[2(\phi_2 - \phi_H)]]. \quad (17)$$

Thus the total average energy at $T = 0$ normalized by K_4 is

$$E_{\text{ave}}/K_4 = (E_{\text{anis ave}} + E_{\text{mag ave}})/K_4$$

$$= -\frac{1}{2} [\cos(4\phi_1) + \cos(4\phi_2)]$$

$$- \frac{\chi_{\perp} H_x^2}{4K_4} [2 + \sin[2(\phi_1 - \phi_H)]$$

$$+ \sin[2(\phi_2 - \phi_H)]]. \quad (18)$$

Here we minimize E_{ave}/K_4 with respect to both $\Delta\phi_1$ and $\Delta\phi_2$ where ϕ_1 and ϕ_2 have maximum values of $\frac{\pi}{4} + \phi_H$ and $\frac{\pi}{4} - \phi_H$, respectively [see Fig. 9(a)]. As can be seen from Fig. 12 for $\phi_H = 1/100$ rad, a discontinuous (first-order) transition is observed for $\Delta\phi_1$ at $H = H_{c1,A}(\phi_H)$, where $\Delta\phi_1$ reaches $\frac{\pi}{4} + \phi_H$ in order for the moments to be perpendicular to H_x at $H_{c1,1}$. On the other hand, no such first-order transition is observed for $\Delta\phi_2$, where $\Delta\phi_2$ instead asymptotes continuously to $\frac{\pi}{4} - \phi_H$ at larger H . The critical field $H_{c1,1}$ is found to decrease and the discontinuity of $\Delta\phi_1$ at $H_{c1,1}$ to increase with increasing ϕ_H . These calculations reveal that when the applied field H_x is not along a crystallographic ab -plane axis, the

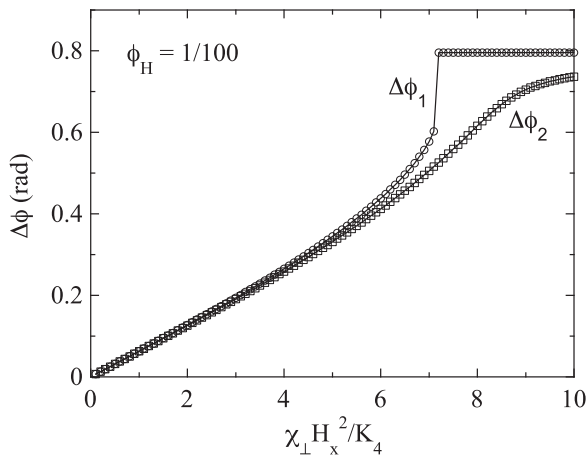


FIG. 12. The angles $\Delta\phi_1$ and $\Delta\phi_2$ in Eqs. (15) vs $\chi_{\perp}H_x^2/K_4$ for $\phi_H = 1/100$ rad. $\Delta\phi_1 = \pi/4$ for $\chi_{\perp}H_x^2/K_4 > 7.1$, whereas $\Delta\phi_2$ eventually asymptotes to $\pi/4$ rad at much larger fields.

field responses of the moments in the two orthogonal domains A and B are quite different. Additional measurements along these lines would be of interest.

V. CONCLUDING REMARKS

The Eu square-lattice compound EuGa_4 exhibits A-type antiferromagnetic order at a Néel temperature $T_N = 16.4(2)$ K with the moments aligned in the ab plane. A magnetic-field-induced anomaly is observed at low fields in the $M_{ab}(H)$ isotherms at $T = 2$ K. We infer that the $H = 0$ A-type magnetic structure consists of four AFM domains associated with a fourfold in-plane magnetic anisotropy, where each domain consists of antiparallel moments in adjacent ab planes along the c axis in zero applied field. On application of an in-plane magnetic field H_x , the collinear moments in each of the AFM domains gradually orient to become perpendicular to H_x at a critical field H_{c1} , yielding a nonlinear $M_{ab}(H)$ at $T = 2$ K. The $M_{ab}(H)$ behavior along the two ab -plane $[1,0,0]$ and $[1,1,0]$ directions are quite different, with respective critical fields $H_{c1,[1,0,0]} = 4.8$ kOe and $H_{c1,[1,1,0]} = 0.85$ kOe. The experimental $M_{ab}(H)$ data for $H \parallel [1, 0, 0]$ and $H \parallel [1, 1, 0]$ were successfully modeled by a theory incorporating the fourfold tetragonal in-plane magnetic anisotropy and associated

AFM domains. However, the calculations predict a first-order transition when the in-plane field H_x is at a finite angle to the $[1,0,0]$ direction. Since the theoretical calculations are done for $T = 0$ K whereas the experiments were performed at 2 K, it would be interesting to calculate the finite temperature effects on the $M(H)$ behavior. In addition, the effects of the Eu-moment rotations for the small magnetic fields discussed here on the topological properties of EuGa_4 would be very interesting to explore.

Similar moment-reorientation effects due to small fields aligned in the ab plane have recently been observed in the trigonal A-type antiferromagnets EuMg_2Bi_2 and EuMg_2Sb_2 containing $S = 7/2$ Eu^{2+} spins with the moments aligned in the ab plane [33]. It seems likely that $M(H)$ measurements for other layered Eu^{2+} or Gd^{3+} spin-7/2 compounds with A-type AFM order and moments aligned in the layer plane would also exhibit low-field effects similar to those described here and in Ref. [33].

As discussed in the Introduction, the skyrmion-like chiral spin texture was initially proposed only in noncentrosymmetric materials with Dzyaloshinskii-Moriya $\mathbf{S}_i \times \mathbf{S}_j$ interactions. The recent discovery of this spin texture even in rare-earth-based centrosymmetric materials suggested the possible role of different types of magnetic anisotropy in those systems. In particular, most of these reported centrosymmetric compounds contain Gd^{3+} with $S = 7/2$ and $L = 0$, yielding negligible single-ion anisotropy. In the absence of this anisotropy it is important to determine the role of other types of anisotropy. The Eu^{2+} ion is isoelectronic to Gd^{3+} with $L = 0$. In our work, the results suggest that in the absence of single-ion anisotropy, magnetic-dipole and/or magnetocrystalline anisotropy play a crucial role in the ab -plane domain formation in EuGa_4 . It would therefore be quite interesting to theoretically study the potential role of such anisotropies in the formation of nontrivial chiral spin textures.

ACKNOWLEDGMENTS

This research was supported by the U.S. Department of Energy, Office of Basic Energy Sciences, Division of Materials Sciences and Engineering. Ames National Laboratory is operated for the U.S. Department of Energy by Iowa State University under Contract No. DE-AC02-07CH11358.

- [1] T. Jungwirth, J. Sinova, A. Manchon, X. Marti, J. Wunderlich, and C. Felser, The multiple directions of antiferromagnetic spintronics, *Nat. Phys.* **14**, 200 (2018).
- [2] B. G. Park, J. Wunderlich, X. Martí, V. Holý, Y. Kurosaki, M. Yamada, H. Yamamoto, A. Nishide, J. Hayakawa, H. Takahashi, A. B. Shick, and T. Jungwirth, A spin-valve-like magnetoresistance of an antiferromagnet-based tunnel junction, *Nat. Mater.* **10**, 347 (2011).
- [3] A. Fert, N. Reyren, and V. Cros, Magnetic Skyrmions: Advances in physics and potential applications, *Nat. Rev. Mater.* **2**, 17031 (2017).
- [4] Y. Tokura and N. Kanazawa, Magnetic skyrmion materials, *Chem. Rev.* **121**, 2857 (2021).
- [5] M. M. Otrokov, I. I. Klimovskikh, H. Bentmann, D. Estyunin, A. Zeugner, Z. S. Aliev, S. Gaß, A. U. B. Wolter, A. V. Koroleva, A. M. Shikin, M. Blanco-Rey, M. Hoffmann, I. P. Rusinov, A. Yu. Vyazovskaya, S. V. Ereemeev, Y. M. Koroteev, V. M. Kuznetsov, F. Freyse, J. Sánchez-Barriga, I. R. Amiraslanov, M. B. Babanly, B. Büchner, G. Di Santo, M. Ünzelmann *et al.*, Prediction and observation of an antiferromagnetic topological insulator, *Nature (London)* **576**, 416 (2019).
- [6] M. C. Rahn, J. R. Soh, S. Francoual, L. S. I. Veiga, J. Strempler, J. Mardegan, D. Y. Yan, Y. F. Guo, Y. G. Shi, and A. T. Boothroyd, Coupling of magnetic order and charge transport in the candidate

- Dirac semimetal EuCd_2As_2 , *Phys. Rev. B* **97**, 214422 (2018).
- [7] M. Hirschberger, S. Kushwaha, Z. Wang, Q. Gibson, S. Liang, C. A. Belvin, B. A. Bernevig, R. J. Cava, and N. P. Ong, The chiral anomaly and thermopower of Weyl fermions in the half-Heusler GdPtBi , *Nat. Mater.* **15**, 1161 (2016).
- [8] T. Kurumaji, T. Nakajima, M. Hirschberger, A. Kikkawa, Y. Yamasaki, H. Sagayama, H. Nakao, Y. Taguchi, T. Arima, and Y. Tokura, Skyrmion lattice with a giant topological Hall effect in a frustrated triangular-lattice magnet, *Science* **365**, 914 (2019).
- [9] N. H. Jo, B. Kuthanazhi, Y. Wu, E. Timmons, T. H. Kim, L. Zhou, L. L. Wang, B. G. Ueland, A. Palasyuk, D. H. Ryan, R. J. McQueeney, K. Lee, B. Schruck, A. A. Burkov, R. Prozorov, S. L. Bud'ko, A. Kaminski, and P. C. Canfield, Manipulating magnetism in the topological semimetal EuCd_2As_2 , *Phys. Rev. B* **101**, 140402(R) (2020).
- [10] S. X. M. Riberolles, T. V. Trevisan, B. Kuthanazhi, T. W. Heitmann, F. Ye, D. C. Johnston, S. L. Bud'ko, D. H. Ryan, P. C. Canfield, A. Kreyssig, A. Vishwanath, R. J. McQueeney, L. L. Wang, P. P. Orth, and B. G. Ueland, Magnetic crystalline-symmetry-protected axion electrodynamics and field-tunable unpinned Dirac cones in EuIn_2As_2 , *Nat. Commun.* **12**, 999 (2021).
- [11] H. Li, S.-Y. Gao, S.-F. Duan, Y.-F. Xu, K.-J. Zhu, S.-J. Tian, J.-C. Gao, W.-H. Fan, Z.-C. Rao, J.-R. Hugang, J.-J. Li, D.-Y. Yan, Z.-T. Liu, W.-L. Liu, Y.-B. Huang, Y.-L. Li, Y. Liu, G.-B. Zhang, P. Zhang, T. Kondo *et al.*, Dirac Surface States in Intrinsic Magnetic Topological Insulators EuSn_2As_2 and $\text{MnBi}_{2n}\text{Te}_{3n+1}$, *Phys. Rev. X* **9**, 041039 (2019).
- [12] T. Shang, Y. Xu, D. J. Gawryluk, J. Z. Ma, T. Shiroka, M. Shi, and E. Pomjakushina, Anomalous Hall resistivity and possible topological Hall effect in the EuAl_4 antiferromagnet, *Phys. Rev. B* **103**, L020405 (2021).
- [13] H. Zhang, X. Y. Zhu, Y. Xu, D. J. Gawryluk, W. Xie, S. L. Ju, M. Shi, T. Shiroka, Q. F. Zhan, E. Pomjakushina, and T. Shang, Giant magnetoresistance and topological Hall effect in the EuGa_4 antiferromagnet, *J. Phys.: Condens. Matter* **34**, 034005 (2022).
- [14] J. M. Moya, S. Lei, E. M. Clements, K. Allen, S. Chi, S. Sun, Q. Li, Y. Y. Peng, A. Husain, M. Mitrano, M. J. Krogstad, R. Osborn, P. Abbamonte, A. B. Puthirath, J. W. Lynn, and E. Morosan, Incommensurate magnetic orders and possible field induced skyrmions in the square-net centrosymmetric EuGa_2Al_2 system, *Phys. Rev. Materials* **6**, 074201 (2022).
- [15] F. Kneidinger, L. Salamakha, E. Bauer, I. Zeiringer, P. Rogl, C. Blaas-Schenner, D. Reith, and R. Podloucky, Superconductivity in noncentrosymmetric BaAl_4 derived structures, *Phys. Rev. B* **90**, 024504 (2014).
- [16] S. Araki, Y. Ikeda, T. C. Kobayashi, A. Nakamura, Y. Hiranaka, M. Hedo, T. Nakama, and Y. Ōnuki, Charge density wave transition in EuAl_4 , *J. Phys. Soc. Jpn.* **83**, 015001 (2014).
- [17] A. Nakamura, Y. Hiranaka, M. Hedo, T. Nakama, Y. Miura, H. Tsutsumi, A. Mori, K. Ishida, K. Mitamura, Y. Hirose, K. Sugiyama, F. Honda, T. Takeuchi, T. D. Matsuda, E. Yamamoto, Y. Haga, and Y. Ōnuki, Unique Fermi surface and emergence of charge density wave in EuGa_4 and EuAl_4 , *JPS Conf. Proc.* **3**, 011012 (2014).
- [18] A. Nakamura, T. Uejo, F. Honda, T. Takeuchi, H. Harima, E. Yamamoto, Y. Haga, K. Matsubayashi, Y. Uwatoko, M. Hedo, T. Nakama, and Y. Ōnuki, Transport and magnetic properties of EuAl_4 and EuGa_4 , *J. Phys. Soc. Jpn.* **84**, 124711 (2015).
- [19] M. Stavinoha, J. A. Cooley, S. G. Minasian, T. M. McQueen, S. M. Kauzlarich, C.-L. Huang, and E. Morosan, Charge density wave behavior and order-disorder in the antiferromagnetic metallic series $\text{Eu}(\text{Ga}_{1-x}\text{Al}_x)_4$, *Phys. Rev. B* **97**, 195146 (2018).
- [20] S. Ramakrishnan, S. R. Kotla, T. Rekiş, J.-K. Bao, C. Eisele, L. Noohinejad, M. Tolkiehn, C. Paulmann, B. Singh, R. Verma, B. Bag, R. Kulkarni, A. Thamizhavel, B. Singh, S. Ramakrishnan, and S. van Smaalen, Orthorhombic charge density wave on the tetragonal lattice of EuAl_4 , *IUCrJ* **9**, 378 (2022).
- [21] A. Nakamura, Y. Hiranaka, M. Hedo, T. Nakama, Y. Miura, H. Tsutsumi, A. Mori, K. Ishida, K. Mitamura, Y. Hirose, K. Sugiyama, F. Honda, R. Settai, T. Takeuchi, M. Hagiwara, T. D. Matsuda, E. Yamamoto, Y. Haga, K. Matsubayashi, Y. Uwatoko, Y. Ōnuki *et al.*, Magnetic and Fermi surface properties of EuGa_4 , *J. Phys. Soc. Jpn.* **82**, 104703 (2013).
- [22] N. D. Khanh, T. Nakajima, X. Yu, S. Gao, K. Shibata, M. Hirschberger, Y. Yamasaki, H. Sagayama, H. Nakao, L. Peng, K. Nakajima, R. Takagi, T. Arima, Y. Tokura, and S. Seki, Nanometric square skyrmion lattice in a centrosymmetric tetragonal magnet, *Nat. Nanotechnol.* **15**, 444 (2020).
- [23] M. Hirschberger, T. Nakajima, S. Gao, L. Peng, A. Kikkawa, T. Kurumaji, M. Kriener, Y. Yamasaki, H. Sagayama, H. Nakao, K. Ohishi, K. Kakurai, Y. Taguchi, X. Yu, T. Arima, and Y. Tokura, Skyrmion phase and competing magnetic orders on a breathing kagomé lattice, *Nat. Commun.* **10**, 5831 (2019).
- [24] S. Hayami and Y. Motome, Square skyrmion crystal in centrosymmetric itinerant magnets, *Phys. Rev. B* **103**, 024439 (2021).
- [25] X. Y. Zhu, H. Zhang, D. J. Gawryluk, Z. X. Zhen, B. C. Yu, S. L. Ju, W. Xie, D. M. Jiang, W. J. Cheng, Y. Xu, M. Shi, E. Pomjakushina, Q. F. Zhan, T. Shiroka, and T. Shang, Spin order and fluctuations in the EuAl_4 and EuGa_4 topological antiferromagnets: A μSR study, *Phys. Rev. B* **105**, 014423 (2022).
- [26] S. Lei, K. Allen, J. Huang, J. M. Moya, B. Casas, Y. Zhang, M. Hashimoto, D. Lu, J. Denlinger, L. Balicas, M. Yi, Y. Sun, and E. Morosan, Weyl nodal ring states and Landau quantization with very large magnetoresistance in square-net magnet EuGa_4 , *arXiv:2208.06407*.
- [27] T. Kawasaki, K. Kaneko, A. Nakamura, N. Aso, M. Hedo, T. Nakama, T. Ohhara, R. Kiyonagi, K. Oikawa, I. Tamura, A. Nakao, K. Munakata, T. Hanashima, and Y. Ōnuki, Magnetic structure of divalent europium Compound EuGa_4 studied by single-crystal time-of-flight neutron diffraction, *J. Phys. Soc. Jpn.* **85**, 114711 (2016).
- [28] M. Yogi, S. Nakamura, N. Higa, H. Niki, Y. Hirose, Y. Ōnuki, and H. Harima, ^{153}Eu and $^{69,71}\text{Ga}$ zero-field NMR study of antiferromagnetic state in EuGa_4 , *J. Phys. Soc. Jpn.* **82**, 103701 (2013).
- [29] D. C. Johnston, Magnetic Susceptibility of Collinear and Non-collinear Heisenberg Antiferromagnets, *Phys. Rev. Lett.* **109**, 077201 (2012).
- [30] D. C. Johnston, Unified molecular field theory for collinear and noncollinear Heisenberg antiferromagnets, *Phys. Rev. B* **91**, 064427 (2015).
- [31] S. Pakhira, M. A. Tanatar, and D. C. Johnston, Magnetic, thermal, and electronic-transport properties of EuMg_2Bi_2 single crystals, *Phys. Rev. B* **101**, 214407 (2020).

- [32] S. Pakhira, T. Heitmann, S. X. M. Riberolles, B. G. Ueland, R. J. McQueeney, D. C. Johnston, and D. Vaknin, Zero-field magnetic ground state of EuMg_2Bi_2 , *Phys. Rev. B* **103**, 024408 (2021).
- [33] S. Pakhira, Y. Lee, L. Ke, and D. C. Johnston, Magnetic-field-induced ab -plane rotation of the Eu magnetic moments in trigonal EuMg_2Bi_2 and EuMg_2Sb_2 single crystals below their Néel temperatures, *Phys. Rev. B* **106**, 184423 (2022).
- [34] S. Pakhira, M. A. Tanatar, T. Heitmann, D. Vaknin, and D. C. Johnston, A-type antiferromagnetic order and magnetic phase diagram of the trigonal Eu spin- $\frac{7}{2}$ triangular-lattice compound EuSn_2As_2 , *Phys. Rev. B* **104**, 174427 (2021).
- [35] S. Pakhira, F. Islam, E. ÓLeary, M. A. Tanatar, T. Heitmann, L. Wang, R. Prozorov, A. Kaminski, D. Vaknin, and D. C. Johnston, A-type antiferromagnetic order in semiconducting EuMg_2Sb_2 single crystals, *Phys. Rev. B* **106**, 024418 (2022).
- [36] K. H. J. Buschow and F. R. de Boer, *Physics of Magnetism and Magnetic Materials* (Klewer/Plenum, New York, 2003), p. 97.
- [37] D. C. Johnston, Magnetic dipole interactions in crystals, *Phys. Rev. B* **93**, 014421 (2016).